

Deep vectorised operators for pulsatile hemodynamics estimation in coronary arteries from a steady-state prior

Julian Suk^{a,*}, Guido Nannini^b, Patryk Rygiel^a, Christoph Brune^a, Gianluca Pontone^{c,d}, Alberto Redaelli^b and Jelmer M. Wolterink^a

^aDepartment of Applied Mathematics and Technical Medical Center, University of Twente, Enschede, The Netherlands

^bDepartment of Electronics Information and Bioengineering, Politecnico di Milano, Milan, Italy

^cDepartment of Perioperative Cardiology and Cardiovascular Imaging, Centro Cardiologico Monzino IRCCS, Milan, Italy

^dDepartment of Biomedical, Surgical and Dental Sciences, University of Milan, Milan, Italy

ARTICLE INFO

Keywords:

Coronary hemodynamics
Computational fluid dynamics
Machine learning
Coronary simulation runtime

ABSTRACT

Cardiovascular hemodynamic fields provide valuable medical decision markers for coronary artery disease. Computational fluid dynamics (CFD) is the gold standard for accurate, non-invasive evaluation of these quantities *in vivo*. In this work, we propose a time-efficient surrogate model, powered by machine learning, for the estimation of pulsatile hemodynamics based on steady-state priors. We introduce deep vectorised operators, a modelling framework for discretisation-independent learning on infinite-dimensional function spaces. The underlying neural architecture is a neural field conditioned on hemodynamic boundary conditions. Importantly, we show how relaxing the requirement of point-wise action to permutation-equivariance leads to a family of models that can be parametrised by message passing and self-attention layers. We evaluate our approach on a dataset of 74 stenotic coronary arteries extracted from coronary computed tomography angiography (CCTA) with patient-specific pulsatile CFD simulations as ground truth. We show that our model produces accurate estimates of the pulsatile velocity and pressure while being agnostic to re-sampling of the source domain (discretisation independence). This shows that deep vectorised operators are a powerful modelling tool for cardiovascular hemodynamics estimation in coronary arteries and beyond.


1. Introduction

Coronary artery disease (CAD) consists in the accumulation of plaque in the artery wall which results in narrowing of the blood vessel. Stenoses then impair the flow of oxygenated blood through the coronary arteries to the heart muscle, which can lead to myocardial infarction (Zingaro, Vergara, Dede, Regazzoni and Quarteroni, 2023). Visualisation and quantification of patient-specific blood flow can be valuable for diagnosis (Driessen, Danad, Stuijffzand, Rajmakers, Schumacher, van Diemen, Leipsic, Knuuti, Underwood, van de Ven, van Rossum, Taylor and Knaapen, 2019), prognosis (Candrea, Pagnoni, Rizzini, Mizukami, Gallinoro, Mazzi, Gallo, Meier, Shinke, Aben, Nagumo, Sonck, Munhoz, Fournier, Barbato, Heggermont, Cook, Chiastra, Morbiducci, De Bruyne, Muller and Collet, 2022) and treatment (Chung and Cebal, 2015) of cardiovascular disease. Quantities derived from the blood flow and pressure, e.g., wall shear stress, oscillatory shear index and fractional flow reserve (trans-stenotic pressure ratio, measured during maximal hyperemia), have been identified as useful decision markers and risk factors in CAD. Computing these biomarkers requires access to pulsatile velocity and pressure fields within the vessel.

Clinical hemodynamic biomarkers can be non-invasively quantified *in-vivo* with imaging techniques such as Doppler ultrasound, particle image velocimetry or 4D flow magnetic resonance imaging (MRI). However, the small size of the

coronary arteries limits the extraction of hemodynamic metrics that can effectively distinguish pathological conditions. Alternatively, these metrics can be obtained *in-silico* via computational fluid dynamics (CFD) based on 3D patient models reconstructed from computed tomography (CT) (Nannini, Saitta, Mariani, Maragna, Baggiano, Mush-taq, Pontone and Redaelli, 2024). Some of the challenges related to clinical adoption of CFD are its long runtimes, high computational demand and dependence on expert knowledge throughout the process. Furthermore, sensitivity to modelling choices, such as *discretisation* of time and space, as well as boundary conditions, make it difficult to decide upon systematic protocols that are consistent and repeatable across hospitals. Indeed, it has been shown that there is inter-operator variability between CFD simulations based on identical medical images (Valen-Sendstad, Bergersen, Shimogonya, Goubergrits, Bruening, Pallares, Cito, Piskin, Pekkan, Geers, Larrabide, Rapaka, Mihalef, Fu, Qiao, Jain, Roller, Mardal, Kamakoti, Spirka, Ashton, Revell, Aristokleous, Houston, Tsuji, Ishida, Menon, Browne, Broderick, Shojima, Koizumi, Barbour, Aliseda, Morales, Lefevre, Hodis, Al-Smadi, Tran, Marsden, Vaip-pummadhom, Einstein, Brown, Debus, Niizuma, Rashad, ichiro Sugiyama, Khan, Updegrove, Shadden, Cornelissen, Majoie, Berg, Saalfeld, Kono and Steinman, 2018). While CFD is gradually making its way into the clinic, pioneered in part by commercial service providers like HeartFlow (Wu, Wu, Theodorou, Liang, Mack, Glass, Sun and Zou, 2024), the above challenges make such services expensive which may hinder widespread adoption.

*Corresponding author

 j.m.suk@utwente.nl (J. Suk)

ORCID(s): 0000-0003-0729-047X (J. Suk)

In this work, we address these challenges with an in-silico surrogate model for estimation of coronary hemodynamics, based on machine learning. We train the model on a dataset of pulsatile CFD simulations, i.e. time-varying velocity and pressure fields, in right and left coronary branches of 74 patients scheduled for clinically indicated invasive coronary angiography for suspected CAD. Additionally, we create a steady-state simulation for each patient, representing the pulsatile CFD solution at the first instant of the cardiac cycle (i.e., at time $t = t_0 + dt$ where t_0 is the end diastolic time) and use them to cast the learning objective as operator learning: we let our neural networks learn a mapping from the steady-state to the corresponding pulsatile hemodynamics. The steady-state CFD solution provides a powerful prior that enables us to faithfully predict the pulsatile hemodynamics even with limited (yet diverse) data.

We name our approach *deep vectorised operators* and lay out a modelling framework in which the nonlinear operator is learned by a vectorised conditional neural field. Relaxing the requirement of point-wise action of neural fields to permutation equivariance allows us to parametrise our models as PointNet++ Qi, Yi, Su and Guibas (2017) and transformers (Vaswani, Shazeer, Parmar, Uszkoreit, Jones, Gomez, Kaiser and Polosukhin, 2017) which have recently proven capable of learning hemodynamics in large-scale, anatomical meshes (Morales Ferez, Mill, Juhl, Acebes, Iriart, Legghe, Cochet, De Backer, Paulsen and Camara, 2021; Suk, Haan, Imre and Wolterink, 2024c). To further facilitate learning from limited amounts of data, we incorporate group equivariance in our models, which can be advantageous for extracting information from small hemodynamic datasets (Suk, Brune and Wolterink, 2023). As in CFD (Lopes, Puga, Teixeira and Lima, 2020), our method is informed by patient-specific boundary conditions. Once trained, our models can quickly produce pressure and velocity field estimates for vascular anatomy on consumer hardware based on boundary conditions for a new patient. We empirically show that our model is robust w.r.t. discretisation of the flow domain.

Our contributions are as follows: (1) we explore learning pulsatile hemodynamics from steady-state priors with a nonlinear operator, (2) we provide a unified modelling framework for neural hemodynamic field estimation with state-of-the-art neural architectures and (3) we evaluate our approach on a relevant, real-life dataset of coronary arteries with patient-specific CFD simulations.

2. Related works

Estimation of hemodynamics with machine learning methods has been an active area of research. Typically, these works fall into one of two categories: (1) transductive instance optimisation with physics-based regularisation (solving partial differential equations) and (2) inductive, generalising feed-forward methods that learn to infer hemodynamics based on patient anatomy and boundary conditions. The former category requires long training times for

each new subject, often in the same order of magnitude as CFD. These methods can be useful in scenarios where hemodynamic parameters are only partially known (Raissi, Yazdani and Karniadakis, 2020; Fathi, Perez-Raya, Baghaie, Berg, Janiga, Arzani and D'Souza, 2020; Kontogiannis and Juniper, 2021). In contrast, methods in the latter category are designed as fast, compute-efficient CFD surrogates.

In this study, we concentrate on the second approach: leveraging neural networks to model the relationship between vascular geometry, boundary conditions and hemodynamic patterns. These neural networks process 3D vessel structures to predict blood-flow-related parameters on the vessel surface or within the interior. In addition to research aimed at predicting 1D quantities along the vessel tree (Pegolotti, Pfaller, Rubio, Ding, Brugarolas Brufau, Darve and Marsden, 2024) and surface characteristics such as wall shear stress (Suk, de Haan, Lippe, Brune and Wolterink, 2024b; Gharleghi, Sowmya and Beier, 2022), pressure drop (Rygiel, Płuszcza, Ziundefinba and Konopczyński, 2023) as well as endothelial cell activation potential (Morales Ferez et al., 2021), several studies have focused on predicting volumetric vector fields. For example, Liang, Mao and Sun (2020) and Wang, Wu, Li, Zhang, Xiao, Li, Qiao, Jin and Liu (2023) trained fully-connected neural networks that work on 3D point-cloud representations of the carotid artery and thoracic aorta, respectively, to predict pressure and velocity fields. Maul, Zinn, Wagner, Thies, Rohleder, Pfaff, Kowarschik, Birkhold and Maier (2023) developed an octree-based neural network, paired with trilinear interpolation to learn parametric, pulsatile flow independently of spatial discretisation and applied it to synthetic vascular trees. Li, Wang, Zhang, Tupin, Qiao, Liu, Ohta and Anzai (2021a) employed a point-cloud-based architecture to estimate pressure and velocity fields in coronary arteries and synthetic cerebral aneurysms. Zhang, Mao, Che, Kang, Luo, Qiao, Liu, Anzai, Ohta, Guo and Li (2023) used a combination of PointNet++ Qi et al. (2017) and a physics-informed neural network (PINN) based on the Navier-Stokes equations to estimate velocity fields in 3D models of the abdominal aorta. In prior work (Suk et al., 2023) we used a multiscale, E(3)-steerable graph neural network to estimate velocity fields in synthetic coronary arteries.

Operator learning approaches, such as DeepONet (Lu, Jin, Pang, Zhang and Karniadakis, 2021) and (Fourier) neural operators (Kovachki, Li, Liu, Azizzadenesheli, Bhattacharya, Stuart and Anandkumar, 2024; Li, Kovachki, Azizzadenesheli, Liu, Bhattacharya, Stuart and Anandkumar, 2021b) have recently gained traction in the machine learning community but there are few applications to cardiovascular hemodynamics estimation.

3. Coronary artery dataset

Patient-specific CFD simulations of coronary flow from a previous study (Nannini et al., 2024) served as the dataset. A brief overview of the data generation process is provided

in the following. Coronary computed tomography angiography (CCTA) scans of patients scheduled for clinically-indicated invasive coronary angiography due to suspected CAD were retrospectively collected from Centro Cardiologico Monzino (Milan, Italy). Overall, 74 stenotic vessel geometries, from both the left (48) and right (26) coronary arteries, were reconstructed from CCTA scans using 3DSlicer (Fedorov, Beichel, Kalpathy-Cramer, Finet, Fillion-Robin, Pujol, Bauer, Jennings, Fennessy, Sonka, Buatti, Aylward, Miller, Pieper and Kikinis, 2012). The segmentation included the artery branches downstream of the ostium, and was terminated when the vessel diameter fell below 1.5 mm, in accordance with established guidelines (Pontone, Moharem-Elgamal, Maurovich-Horvat, Gaemperli, Pugliese, Westwood, Stefanidis, Fox and Popescu, 2017). The aortic root was excluded. The study was performed in accordance with recommendations of the local Ethics Committee, with written informed consent from all subjects, in accordance with the Declaration of Helsinki.

The volume of the reconstructed geometries was discretized into tetrahedral elements with a characteristic size of 0.25 mm using the TetGen algorithm embedded within SimVascular (Updegrave, Wilson, Merkow, Lan, Marsden and Shadden, 2017). This led to 1,801,029 tetrahedral elements and 314,525 vertices on average. For each mesh, three cardiac cycles were simulated by numerically solving the incompressible Navier-Stokes equations, with time-varying boundary conditions, in SimVascular. A time discretization of $dt = 0.001$ seconds was adopted in the CFD, results were exported every 0.025 seconds, which corresponds to the largest time step value that ensured the numerical convergence of the simulation (based on separately run sample-tests). Results were retained solely from the last cycle, spanning 35 time steps on average.

To set up the simulation, the average hyperemic flow rate, \bar{Q}_{hyp} , was computed from baseline clinical measurements and used to scale a flow rate waveform obtained from the literature (Flemister, Hatoum, Guhan, Zebhi, Lincoln and Crestanello, 2020), which was applied as the inlet boundary condition (BC) $Q_{hyp}(t)$ in the simulation. A five-element Windkessel model was coupled to each outlet as the BC, with its parameters tuned based on the patient's aortic pressure (for further details on the CFD settings, see (Nannini et al., 2024)). Pulsatile simulations took between 12 to 24 h per case.

Additionally, a steady-state CFD simulation was performed for each model using the inflow value corresponding to the flowrate at the first pulsatile-CFD solution output: $Q_{hyp}(t = 0.025)$. We chose this initial time point for the steady-state simulation to minimize inertial effects, which can influence the pressure field in pulsatile CFD simulations. Steady-state simulations took between 5 to 30 min depending on the flow rate where computational cost scaled roughly with the Reynolds number.

4. Background

In the following, we will discuss the relevant theoretical background to put our approach into context. However, our method can be understood independently of this section.

In this work we consider the problem of learning time-dependent, c -dimensional vector fields ($c \in \mathbb{N}$) from data

$$y: \begin{cases} T \times \Omega \rightarrow \mathbb{R}^c \\ t, x \mapsto y(t, x) \end{cases} \quad T \subset \mathbb{R}, \quad \Omega \subset \mathbb{R}^3,$$

which are defined on a time interval T and spatial domain Ω . In the following we propose a family of models that can efficiently represent specific instances of such vector fields while enabling zero-shot *generalisation* to instances beyond the training data. In contrast to common applications in medical imaging, we do not assume the data to have grid structure that we can exploit, e.g., via convolutional neural networks (CNN). Rather, our model learns a map between infinite-dimensional function spaces.

4.1. Neural fields

A neural field is a parametrised map $f_\theta: \mathbb{R}^{c_{in}} \rightarrow \mathbb{R}^{c_{out}}$ between vector spaces where f_θ is a neural network with parameters θ , e.g., a multilayer perceptron (MLP). The domain $\mathbb{R}^{c_{in}}$ is commonly required to be spacetime (Xie, Takikawa, Saito, Litany, Yan, Khan, Tombari, Tompkin, Sitzmann and Sridhar, 2022). The neural network f_θ is trained under observations $\{(x^i \in \mathbb{R}^{c_{in}}, y^i \in \mathbb{R}^{c_{out}})\}_{i \in [1, n]}$ of input-output pairs. Since neural networks are commonly continuous or continuously differentiable, neural fields can be smooth representations of scalar and vector fields in a variety of applications, such as neural signed distance functions (Gropp, Yariv, Haim, Atzmon and Lipman, 2020) and physics-informed neural networks Raissi, Perdikaris and Karniadakis (2019).

4.1.1. Conditional neural fields

Neural fields can be conditioned on a collection of parameters $\xi \in \Xi$, e.g., by concatenating (\parallel) them with the input observations and feeding them to the neural network

$$f_\theta: \begin{cases} \mathbb{R}^{c_{in}} \times \Xi \rightarrow \mathbb{R}^{c_{out}} \\ x, \xi \mapsto f_\theta(x \parallel \xi) \end{cases}.$$

This enables, e.g., representing multiple vector fields with the same domain and co-domain in a single neural field by assigning each vector field a latent code, as proposed by DeepSDF (Park, Florence, Straub, Newcombe and Lovegrove, 2019), or representing *parametric* solutions to partial differential equations. In this case, observations depend on the parameters ξ under which they were made.

4.1.2. Vectorised conditional neural fields

When training conditional neural fields, input observations x^i are commonly vectorised into an $(n \times c_{in})$ -dimensional tensor while f_θ (conditioned on ξ) broadcasts over the batch dimension. Accordingly, f_θ must act point-wise, i.e., row-wise on the input tensor. However, if we

always feed observations to the neural field as complete sets, we can relax this requirement and choose f_θ – instead of point-wise – as point-wise *permutation-equivariant*. Such models allow introducing inter-observation context and thus implicit conditioning on the complete set of observations. Based on the same idea, Hagnberger, Kalimuthu, Musekamp and Niepert (2024) proposed this family of models under the name “vectorised conditional neural fields”.

4.2. Permutation-equivariant neural networks

Permutation-equivariant functions satisfy the condition

$$(f_\theta \circ P)(\cdot) \equiv (P \circ f_\theta)(\cdot) \quad \text{for all } P \in S_n,$$

where \circ denotes composition and S_n is the symmetric group of permutations on n set elements. In other words, the relation between input and output elements cannot depend on their specific ordering. Note that point-wise functions are trivially permutation-equivariant. Among the most popular permutation-equivariant building blocks for neural network composition are message passing and self-attention.

4.2.1. Message passing

In this work we consider message passing on point clouds. Message passing layers act on local neighbourhoods \mathcal{N}_p around points p in the input vector space by constructing messages and updating point features h^p

$$\begin{aligned} m_{p,q} &= \text{MLP}(h^p \parallel h^q \parallel p \parallel q), \quad (\text{message from } q \text{ to } p) \\ h^p &\leftarrow \bigoplus_{q \in \mathcal{N}_p} m_{p,q} \quad (\text{point feature update}) \end{aligned}$$

where \bigoplus is an aggregation operator like mean or maximum. Permutation equivariance is enabled by the dependence of the local neighbourhoods \mathcal{N}_p on the input vector space.

4.2.2. Self-attention

Given an $(n \times c_{\text{in}})$ -dimensional tensor x , multi-head self-attention layers can be defined as follows:

$$\begin{aligned} a_i &= \text{Softmax} \left(\frac{q_i(x) k_i(x)^T}{\sqrt{c_{\text{in}}}} \right) v_i(x) \\ A &= x + \text{Linear} \left(\parallel a_i \right) \\ x &\leftarrow A + \text{MLP}(A), \end{aligned}$$

where Softmax acts entry-wise and we require query, key and value functions q_i, k_i, v_i as well as Linear and MLP to be row-wise permutation-equivariant. Self-attention is a composition of permutation-equivariant operations and computes pair-wise interactions between all n set elements.

4.3. E(3)-equivariant neural networks

Apart from being equivariant under permutations of set elements, neural networks can be equivariant under element-wise rotation, translation and reflection in the input vector space \mathbb{R}^3 if they satisfy the condition

$$(f_\theta \circ \rho)(\cdot) \equiv (\rho \circ f_\theta)(\cdot) \quad \text{for all } \rho \in E(3).$$

In other words, the relation between input and output elements cannot depend on their specific location and orientation in ambient space. All possible rotations, translations and reflections constitute the Euclidean group $E(3)$.

4.4. DeepONet and MIONet

DeepONet (Lu et al., 2021) and its extension MIONet (Jin, Meng and Lu, 2022) are frameworks for learning operators between function spaces. Let γ be a source and y be a target function. The objective is to learn an operator $G_\gamma: \mathbb{R}^{c_{\text{in}}} \rightarrow \mathbb{R}^{c_{\text{out}}}$ so that $G_\gamma(x) \equiv y(x)$. MIONet generalises this to multiple source functions which may include boundary conditions ξ , i.e.,

$$G_{\gamma,\xi}(x) \equiv y_\xi(x).$$

Learning this operator is realised by feeding observations of the input functions to “branch” networks b_1, b_2 and coordinates x to a “trunk” network τ and multiplying their outputs entry-wise:

$$G_{\gamma,\xi}(x) = \text{Sum} (b_1 (\{\gamma^i\}_{i \in [1,n]}) \odot b_2 (\{\xi^i\}_{i \in [1,l]}) \odot \tau(x))$$

where Sum denotes summations of all vector entries and \odot is the Hadamard product. Optionally, a bias term can be added.

5. Methods

5.1. Deep vectorised operator

In this work, we propose a model that takes as inputs steady-state hemodynamic fields as well as pulsatile boundary conditions and estimates the pulsatile hemodynamic fields. Let Ω be the artery and denote by u, p velocity and pressure, respectively. Define the steady-state hemodynamic fields as

$$\gamma: \begin{cases} \Omega \rightarrow \mathbb{R}^3 \times \mathbb{R} \\ x \mapsto u \parallel p \end{cases}$$

and the pulsatile hemodynamic fields as

$$y_\xi: \begin{cases} T \times \Omega \rightarrow \mathbb{R}^3 \times \mathbb{R} \\ t, x \mapsto u_\xi \parallel p_\xi \end{cases}, \xi \in \Xi$$

where Ξ is the function space of all pulsatile boundary conditions described by three quantities: velocity, pressure at the artery inlet and pulsatile waveform. We allow ξ to be dependent on t which we omit for compactness of notation. Conceptually, our model is in between MIONet and (vectorised) conditional neural fields. Our objective is to learn an operator

$$G_{\gamma,\xi}: T \times \Omega \rightarrow \mathbb{R}^3 \times \mathbb{R} \quad \text{so that} \quad G_{\gamma,\xi}(x) \equiv y_\xi(x).$$

We do so via a conditional neural field f_θ so that point-wise

$$G_{\gamma,\xi}(t, x) = f_\theta(\gamma(x) \parallel t \parallel r(x) \parallel \xi)$$

where $r(x)$ is fixed, relational encoding of coordinates which we describe below. We train f_θ on tuples of observations

$$\{(\gamma(x^j), t^i, x^j, y_\xi(t^i, x^j)) \mid i \in [1, m], j \in [1, n]\}$$

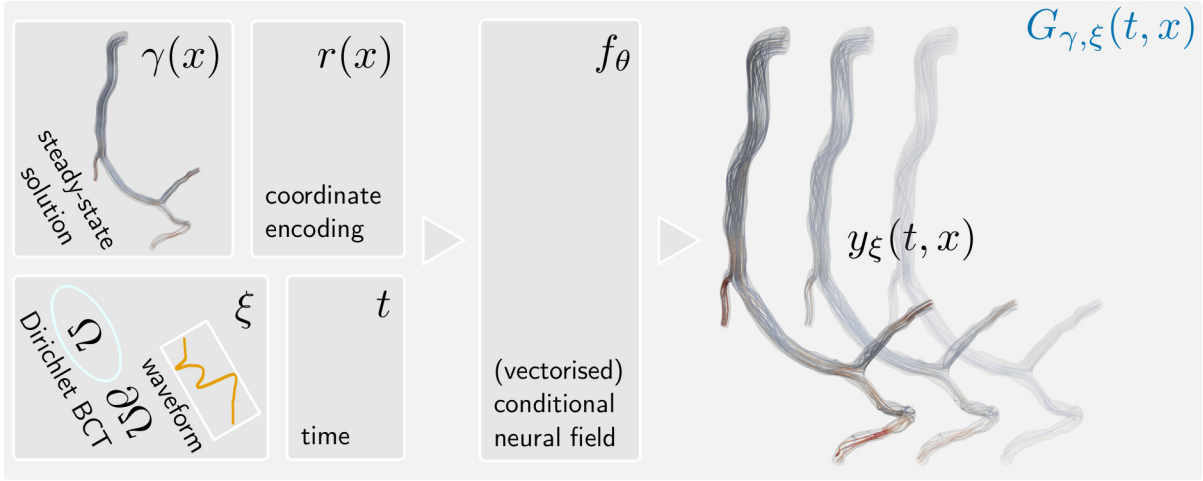


Figure 1: Deep vectorised operator. Steady-state hemodynamic fields $\gamma(x)$ and relational point encoding $r(x)$ are fed to a permutation-equivariant model f_θ together with conditions ξ and query time t . Functional quantities $\gamma(x)$ and $r(x)$ can be vectorised, i.e., supplied all at once, to enable cross-conditioning by parametrising f_θ with message passing or self-attention layers. In that case, global quantities ξ and t are broadcast over the batch dimension. Neural field f_θ then predicts pulsatile hemodynamics $y_\xi(t, x)$ at (each of) the query point(s) (t, x) in spacetime. This defines the nonlinear operator $G_{\gamma, \xi}(t, x)$.

in a vectorised manner. Thus, we can introduce spatial context by allowing f_θ to be permutation-equivariant. This setup can also be viewed as a time-continuous, space-discrete, conditional neural field.

5.1.1. Backend variants

Conditional (vectorised) neural field f_θ can be embodied by a plethora of neural architectures. When designing neural networks for large-scale hemodynamic problems, it is imperative that the models are scalable in the number of query points w.r.t. computation complexity and device usage. We choose a simple, point-wise MLP, the permutation-equivariant PointNet++ and the permutation- as well as SE(3)-equivariant LaB-GATr (Suk, Imre and Wolterink, 2024d; Suk et al., 2024c) with memory-efficient attention (Rabe and Staats, 2021). We also include LaB-VaTr, which uses the same layout as LaB-GATr but vanilla fully-connected layers instead of geometric algebra.

5.1.2. Coordinate encoding

We equip our model with a powerful coordinate space by lifting x^j to a higher-dimensional, relational encoding $r(x^j)$ of spatial location. To this end, we compute – for every point x^j within the artery – relative position to the inlet, closest outlet and inner lumen wall (Suk et al., 2023). We separate these vectors into magnitude and direction, both of which we feed to f_θ . Furthermore, we employ a geometry-aware location descriptor in the form of *diffusion distance* and direction to inlet and outlets. For this we use the heat method for distance computation (Crane, Weischedel and Wardetzky, 2017), originally developed for geodesic distance on surfaces, which readily transfers to volumetric point clouds. The heat method works with a point cloud Laplacian to define an analogue to the heat equation. We can then “simulate” diffusion of heat sources placed at the

inlet and outlets, respectively, and treat the resulting heat map as distance field. To obtain the “direction” of diffusion, we simply take the gradient of said field via the discretisation scheme described in (Suk, Alblas, Hutten, Wiegman, Brune, van Ooij and Wolterink, 2024a).

5.1.3. Boundary condition encoding

As conditions ξ , we supply to our model at each point in time t the average velocity vector over the inlet, decomposed into magnitude and direction, along with the average pressure over the inlet. We assume access to both these quantities because they can readily be measured in hospitals. Additionally, we assume access to a patient-specific blood flow waveform of which we query the mean, standard deviation, minimum and maximum value over the cardiac cycle, which we feed to our model along with the subject’s heart rate.

5.1.4. Pressure drop estimation

Instead of estimating point-wise pressure $p(t, x)$ directly, we found it beneficial to predict the *pressure drop* relative to the pressure at the inlet.

5.2. Evaluation metrics

To evaluate our method, we must compare vector fields, i.e., point-wise model predictions $f_\theta(\dots) =: f_\theta^p$ and ground truth $y_\xi(\dots) =: y_\xi^p$. We do so via the following metrics. We define approximation disparity

$$\text{Approx. disp.} : \sum_p \|y_\xi^p - f_\theta^p\|_2^2 / \sum_p \|y_\xi^p\|_2^2$$

which measures the similarity between the vector fields. Furthermore, we use mean cosine similarity between vectors

$$\text{Cos. similarity} : \text{mean}_p \cos \angle(y_\xi^p, f_\theta^p)$$

Table 1

Quantitative evaluation of backends. We report mean \pm standard deviation (across time and subjects) of Approx. disp. and Cos. similarity w.r.t. hemodynamics $u \parallel p$ jointly, as well as velocity u and pressure p separately. We denote in **bold** best evaluation metrics where they significantly ($p < 0.05$) differ from the next best (one-way ANOVA test). Additionally, we state each model’s training complexity.

Backend	Train. complex.	$u \parallel p$		u		p	
		Approx. disp. \downarrow	Approx. disp. \downarrow	Cos. similarity \uparrow	Approx. disp. \downarrow		
MLP	254 s/epoch	0.432 \pm 0.065	0.439 \pm 0.066	0.72 \pm 0.05	0.121 \pm 0.068		
PointNet++	164 s/epoch	0.382 \pm 0.073	0.388 \pm 0.073	0.76 \pm 0.04	0.115 \pm 0.075		
LaB-GATr	857 s/epoch*	0.368 \pm 0.079	0.374 \pm 0.080	0.76 \pm 0.04	0.105 \pm 0.049		
LaB-VaTr	191 s/epoch	0.402 \pm 0.076	0.409 \pm 0.076	0.74 \pm 0.04	0.098 \pm 0.072		

*on four devices in parallel

which ranges between -1 (opposite) and 1 (proportional) and measures directional agreement independent of magnitude.

6. Experiments and results

6.1. Implementation

We implemented all neural networks in Python using PyTorch (Paszke, Gross, Massa, Lerer, Bradbury, Chanan, Killeen, Lin, Gimelshein, Antiga, Desmaison, Köpf, Yang, DeVito, Raison, Tejani, Chilamkurthy, Steiner, Fang, Bai and Chintala, 2019) and PyTorch Geometric (Fey and Lenssen, 2019). For PointNet++, we opted for an aggressive sampling strategy with cumulative factors of 0.0033, 0.3344, 0.6656 and 0.9967 to account for the large-scale data. Likewise, we chose a compression ratio of 0.0033 for LaB-GATr and LaB-VaTr. We let LaB-GATr use cross-attention for the compression module and LaB-VaTr message passing. We chose these settings since they resulted in favourable runtime and accuracy. We chose hidden channels size so all networks had approximately 0.65 million trainable parameters. We used PyTorch just-in-time compilation to speed up training for MLP while the other models did not benefit from it due to unsupported software.

6.2. Training details

We split the 74 patient-specific CFD simulations into 55 training, 4 validation and 15 test cases. We ensured that training and test split had the same ratio between left and right coronary arteries. Left and right coronary artery of the same subject were considered separate cases. Where the dataset contained geometries of the left as well as the right coronary artery of the same subject, both were included in the same dataset split. All models were trained with batch size 12 (enabled by gradient accumulation) on NVIDIA L40 (48 GB) GPUs using Adam optimiser (learning rate $3 \cdot 10^{-4}$). We trained MLP, PointNet++ and Lab-VaTr each for 1000 epochs on a single GPU which took 56:28 h on average. We trained LaB-GATr for 200 epochs (47:00 h) on four parallel GPUs to ensure fair comparison. For each neural network, we performed two training runs, with and without (both) exponential learning rate decay and gradient

clipping. LAB-GATr showed increased accuracy while the other models did not benefit from it. Our implementation is publicly available.¹

6.3. Hemodynamics estimation

Figure 2 compares the estimated pulsatile hemodynamics by our deep vectorised operator $G_{\gamma, \xi}$ in a patient from the test split to CFD. Here, $G_{\gamma, \xi}$ uses LaB-GATr as backend. From the streamlines, we see good overall agreement between ground truth and prediction. We observe the highest disparity in regions with high-frequency flow components, e.g., around the bifurcation and along the tortuous downstream vasculature during peak systole (time steps four and five). Looking at the pressure maps, we observe excellent agreement between $G_{\gamma, \xi}$ and CFD in upstream vasculature which slightly and gradually decreases moving downstream (compare again peak systole). This might be because we prescribe boundary conditions ξ exclusively at the artery inlet in $G_{\gamma, \xi}$, since it is easier to measure in a clinical scenario.

6.4. Backend study

In Table 1 we compare model predictions on the held-out test split to the corresponding ground truth values via Approx. disp. and Cos. similarity. LaB-GATr achieves the highest accuracy on the estimation of $u \parallel p$, followed by PointNet++, LaB-VaTr and MLP with statistically significant ($p < 0.05$ in a one-way ANOVA test) difference. When isolating the target fields, PointNet++ and LaB-GATr are tied for most accurate (directional) velocity prediction in terms of Cos. similarity while LaB-GATr achieves lower Approx. disp.. LaB-VaTr achieves the lowest mean Approx. disp. in pressure field estimation, however, there is no statistically significant difference to LaB-GATr. In terms of training complexity, PointNet++ is the fastest at 164 seconds per epoch, outpacing MLP despite just-in-time compilation. LaB-GATr is computationally heavy to train, requiring 857 seconds per epoch even when parallelised across four GPUs.

¹github.com/available-upon-publication

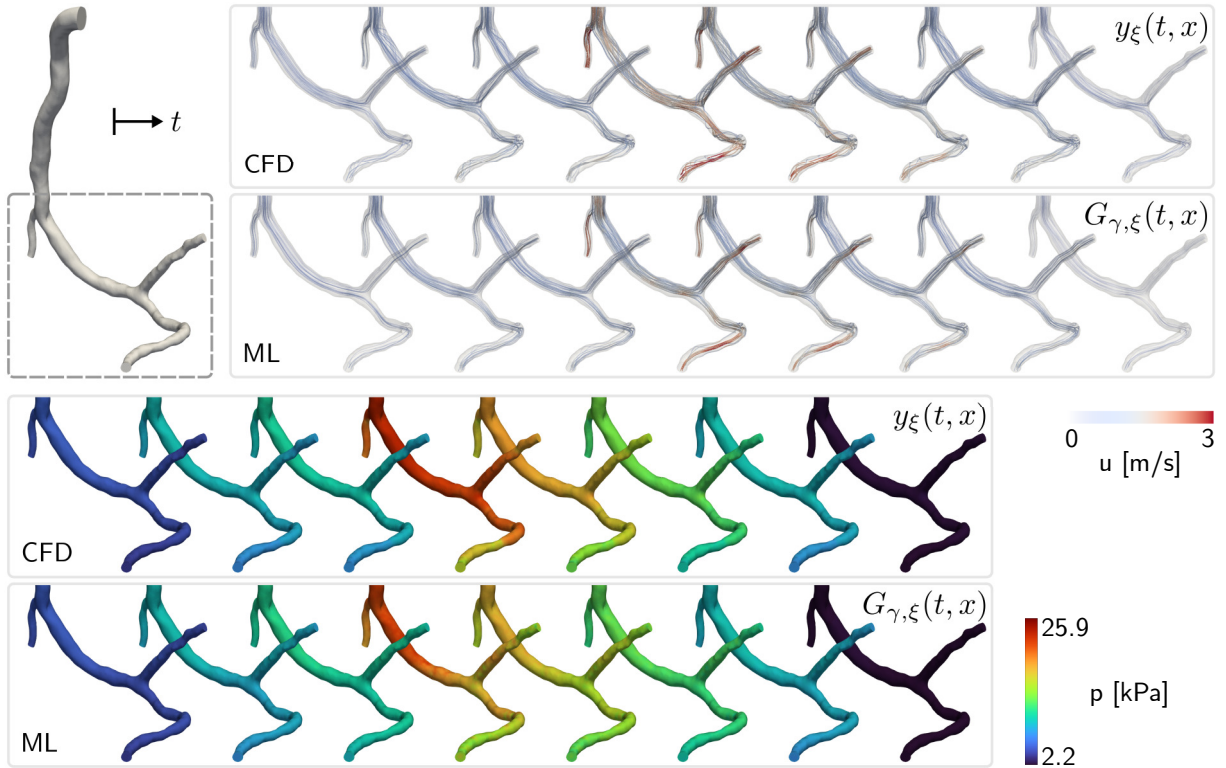


Figure 2: Qualitative evaluation of machine learning (ML) model $G_{\gamma, \xi}(t, x)$ in comparison to CFD $y_{\xi}(t, x)$ in a test subject (generalisation). Approx. disp. associated with $u \parallel p$ estimation in this subject was 0.325. We visualise streamlines and pressure maps for eight time points in the cardiac cycle with spacing $\Delta t = 0.125$ s. The backend model was LaB-GATr.

Table 2

Multitask versus isolated training target. We re-trained PointNet++ three times to predict only velocity u , only pressure p and both $u \parallel p$ jointly and report the resulting metrics.

Training target	u		p
	Approx. disp. ↓	Cos. similarity ↑	Approx. disp. ↓
$u \parallel p$	0.386 ± 0.072	0.76 ± 0.04	0.114 ± 0.073
u	0.388 ± 0.074	0.76 ± 0.04	0.345 ± 0.148
p	1.006 ± 0.018	-0.16 ± 0.12	0.113 ± 0.068

6.5. Multitask versus isolated target learning

We investigate the possible advantage of isolating the estimation of velocity and pressure into separately trained neural networks. To this end, we re-trained a model with the PointNet++ backend for 400 epochs three times, with prediction target $u \parallel p$ (jointly), as well as u and p (isolated). In Table 2 we present the results. We did not find statistically significant ($p < 0.05$ in a one-way ANOVA test) difference between multitask and isolated target learning, indicating that multitask learning neither benefits nor harms prediction of velocity or pressure fields.

6.6. Sensitivity to discretisation

We investigate our models' capability for zero-shot generalisation to re-discretisation of the domain. To this end, we discard the mesh vertices and sample new positions (freely in

space), approximately evenly from the surface of the artery and from within the artery lumen. We make sure the number of sampled surface and volume points are approximately equal to the CFD meshes used during training. We then evaluate the pre-trained (vectorised) conditional neural field f_{θ} with MLP, PointNet++, LaB-GATr and LaB-VaTr as backends on these newly sampled points. To enable comparison to the ground truth, we perform proportional interpolation of steady state and pulsatile hemodynamic fields γ, y_{ξ} based on distance to four closest points in the source mesh.

In Table 3 we report Δ Approx. disp. (the difference in Approx. disp.) between training resolution and randomly sampled points in subjects from the test split. Positive values mean that Approx. disp. increased, i.e., accuracy decreased. We find that for all four backends Δ Approx. disp. is marginal. Furthermore, we find that for MLP, LaB-GATr and LaB-VaTr, the difference is not statistically significant ($p > 0.05$ in a one-way ANOVA test), i.e., re-discretisation has not change their accuracy. The PointNet++ backend is the only one resulting in statistically significant Δ Approx. disp..

Figure 3 showcases the discretisation-robustness of (vectorised) conditional neural field $f_{\theta} = G_{\gamma, \xi}$ for the example of velocity field estimation. Here, f_{θ} uses LaB-GATr as backend. We observe that the vector fields resulting from evaluation of $G_{\gamma, \xi}(t, x)$ on positions x from the CFD mesh (training discretisation) and randomly sampled positions visually coincide. The amount of outliers is negligible.

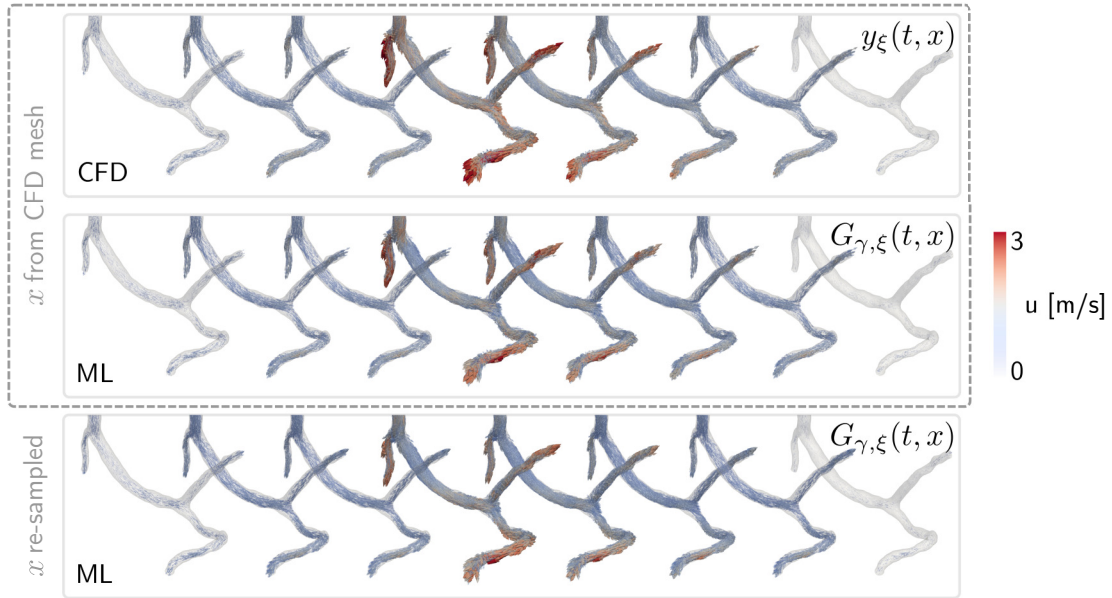


Figure 3: Discretisation sensitivity analysis of machine learning (ML) model in a test subject (generalisation). We evaluate $G_{\gamma, \xi}(t, x)$ on positions x induced by the CFD mesh as well randomly sampled positions from the domain and visualise the resulting velocity fields. The backend model was LaB-GATr.

Table 3

Discretisation sensitivity. We evaluate the pre-trained models on new point coordinates that are randomly sampled from the domain. We report the difference Δ in Approx. disp. for joint prediction of $u \parallel p$ and check whether the difference is statistically significant (one-way ANOVA test).

Backend	$u \parallel p$	
	Δ	Approx. disp. ↓
MLP	-0.004	
PointNet++	+0.021*	
LaB-GATr	-0.000	
LaB-VaTr	-0.003	

*significant ($p < 0.05$)

7. Discussion and conclusion

In this work, we presented a novel deep learning approach that takes the end-diastolic steady-state hemodynamics in the coronary arteries and estimates the corresponding pulsatile hemodynamics, over the full cardiac cycle. This idea is based on the observation that steady-state simulations are orders of magnitude faster than pulsatile simulations while many medically relevant biomarkers are related to pulsatile flow, e.g., multi-directional wall shear stress. Our model is conditioned on the patient-specific pulsatile waveform, as well as the flow and pressure over the artery inlet. All of these quantities are easily accessible from direct or indirect clinical measurements. We evaluated our method on a dataset of CFD-based hemodynamic simulations in stenotic left and right coronary arteries encompassing 74

cases across a cohort of real-life patients. By casting the learning objective as operator learning from steady-state to pulsatile flow, our method is able to accurately capture the 4D nature of blood flow based on limited amounts of (fairly diverse) data. Steady-state simulations were 24 to 288 times faster than pulsatile simulations in these subjects. Consequently, our approach could potentially be useful in the clinic to make pulsatile hemodynamic fields available in settings where time is critical or computational resources are limited. Medical decision markers like wall shear stress, oscillatory shear index and fractional flow reserve can then be computed from pressure and velocity fields. Importantly, our method is robust w.r.t. discretisation of the flow domain which could be beneficial for inter-operator variability.

We described this approach in a unified framework which we called deep vectorised operator, since our model maps between infinite-dimensional function spaces. Deep vectorised operators are parametrised by (vectorised) conditional neural fields Hagnberger et al. (2024) that can be embodied by several backends, as long as they are point-wise permutation-equivariant like message passing or self-attention models. Importantly, *vectorised* neural fields differ from neural fields in the sense that all query points are fed to the model at once, in a vectorised way. Our empirical evidence justifies the nomenclature “neural field” by suggesting that deep vectorised operators are discretisation-independent, i.e., enable zero-shot generalisation to re-sampling of the domain. This is remarkable, because the neural architectures we tested, in particular PointNet++ Qi et al. (2017), are based on cross-conditioning between the query points. Our evidence suggests that they nevertheless function as a mapping between domain and co-domain, just like traditional neural fields Xie et al. (2022) parametrised

by point-wise neural architectures like MLP. As expected, the deep vectorised operator with MLP as backend was agnostic to re-sampling of the domain while PointNet++ exhibited small (but statistically significant) sensitivity, hinting at pronounced cross-conditioning.

Our approach is similar in scope to DeepONet and MIONet as we are learning a deep operator between function spaces. In comparison to MIONet, we sacrificed the entry-wise Hadamard-product structure for scalability and ease of implementation. This affects the learned operator and in turn the available mathematical approximation theory, investigating which is an interesting avenue for future work. In comparison to Maul et al. (2023), our work explores the incorporation of steady-state hemodynamics as powerful prior for pulsatile hemodynamics, our model returns velocity *and* pressure and our dataset is composed of real-life patients. For future work, we plan to incorporate a balance term for inlet and outlet flux in the training loss to improve estimations at the artery outlets, as well as continuity and momentum terms. Furthermore, we will investigate the quality of extracted medical decision markers like wall shear stress, oscillatory shear index and fractional flow reserve computed from deep vectorised operators' estimated hemodynamic fields.

In conclusion, deep vectorised operators can be used to estimate pulsatile from steady-state hemodynamics in coronary arteries while being independent of the discretisation of the domain. Furthermore, deep vectorised operators are a useful modelling tool with many expected applications in cardiovascular medicine and biomedical engineering.

References

- Candrea, A., Pagnoni, M., Rizzini, M.L., Mizukami, T., Gallinoro, E., Mazzi, V., Gallo, D., Meier, D., Shinke, T., Aben, J.P., Nagumo, S., Sonck, J., Munhoz, D., Fournier, S., Barbato, E., Heggermont, W., Cook, S., Chiastra, C., Morbiducci, U., De Bruyne, B., Muller, O., Collet, C., 2022. Risk of myocardial infarction based on endothelial shear stress analysis using coronary angiography. *Atherosclerosis* 342, 28–35.
- Chung, B., Cebal, J.R., 2015. CFD for evaluation and treatment planning of aneurysms: review of proposed clinical uses and their challenges. *Annals of Biomedical Engineering* 43, 122–138.
- Crane, K., Weischedel, C., Wardetzky, M., 2017. The heat method for distance computation. *Commun. ACM* 60, 90–99.
- Driessen, R.S., Danad, I., Stuijzand, W.J., Raijmakers, P.G., Schumacher, S.P., van Diemen, P.A., Leipsic, J.A., Knuuti, J., Underwood, S.R., van de Ven, P.M., van Rossum, A.C., Taylor, C.A., Knaapen, P., 2019. Comparison of coronary computed tomography angiography, fractional flow reserve, and perfusion imaging for ischemia diagnosis. *Journal of the American College of Cardiology* 73, 161–173.
- Fathi, M.F., Perez-Raya, I., Baghaie, A., Berg, P., Janiga, G., Arzani, A., D'Souza, R.M., 2020. Super-resolution and denoising of 4D-flow mri using physics-informed deep neural nets. *Computer Methods and Programs in Biomedicine* 197, 105729.
- Fedorov, A., Beichel, R., Kalpathy-Cramer, J., Finet, J., Fillion-Robin, J.C., Pujol, S., Bauer, C., Jennings, D., Fennessy, F., Sonka, M., Buatti, J., Aylward, S., Miller, J.V., Pieper, S., Kikinis, R., 2012. 3D Slicer as an image computing platform for the Quantitative Imaging Network. *Magnetic resonance imaging* 30, 1323–1341.
- Fey, M., Lenssen, J.E., 2019. Fast graph representation learning with PyTorch Geometric, in: *ICLR Workshop on Representation Learning on Graphs and Manifolds*, p. 0–9.
- Flemister, D.C., Hatoum, H., Guhan, V., Zebhi, B., Lincoln, J., Crestanello, Juan Dasi, L.P., 2020. Effect of Left and Right Coronary Flow Waveforms on Aortic Sinus Hemodynamics and Leaflet Shear Stress: Correlation with Calcification Locations. *Annals of Biomedical Engineering* 48, 2796–2808.
- Gharleghi, R., Sowmya, A., Beier, S., 2022. Transient wall shear stress estimation in coronary bifurcations using convolutional neural networks. *Computer Methods and Programs in Biomedicine* 225, 107013.
- Gropp, A., Yariv, L., Haim, N., Atzmon, M., Lipman, Y., 2020. Implicit geometric regularization for learning shapes, in: *Proceedings of the 37th International Conference on Machine Learning, JMLR.org*. pp. 0–11.
- Hagnberger, J., Kalimuthu, M., Musekamp, D., Niepert, M., 2024. Vectorized conditional neural fields: A framework for solving time-dependent parametric partial differential equations, in: *Forty-first International Conference on Machine Learning, ICML 2024, Vienna, Austria, July 21-27, 2024, OpenReview.net*. pp. 0–35.
- Jin, P., Meng, S., Lu, L., 2022. Mionet: Learning multiple-input operators via tensor product. *SIAM Journal on Scientific Computing* 44, A3490–A3514.
- Kontogiannis, A., Juniper, M., 2021. Physics-informed compressed sensing: reconstruction of magnetic resonance velocimetry signals as an inverse Navier-Stokes problem, in: *APS Division of Fluid Dynamics Meeting Abstracts*, p. H20.001.
- Kovachki, N., Li, Z., Liu, B., Azizzadenesheli, K., Bhattacharya, K., Stuart, A., Anandkumar, A., 2024. Neural operator: learning maps between function spaces with applications to pdes. *J. Mach. Learn. Res.* 24.
- Li, G., Wang, H., Zhang, M., Tupin, S., Qiao, A., Liu, Y., Ohta, M., Anzai, H., 2021a. Prediction of 3D cardiovascular hemodynamics before and after coronary artery bypass surgery via deep learning. *Communications Biology* 4.
- Li, Z., Kovachki, N.B., Azizzadenesheli, K., Liu, B., Bhattacharya, K., Stuart, A.M., Anandkumar, A., 2021b. Fourier neural operator for parametric partial differential equations, in: *9th International Conference on Learning Representations, ICLR 2021, Virtual Event, Austria, May 3-7, 2021, OpenReview.net*. pp. 0–16.
- Liang, L., Mao, W., Sun, W., 2020. A feasibility study of deep learning for predicting hemodynamics of human thoracic aorta. *Journal of Biomechanics* 99, 109544.
- Lopes, D., Puga, H., Teixeira, J., Lima, R., 2020. Blood flow simulations in patient-specific geometries of the carotid artery: A systematic review. *Journal of Biomechanics* 111, 110019.
- Lu, L., Jin, P., Pang, G., Zhang, Z., Karniadakis, G.E., 2021. Learning nonlinear operators via DeepONet based on the universal approximation theorem of operators. *Nat. Mach. Intell.* 3, 218–229.
- Maul, N., Zinn, K., Wagner, F., Thies, M., Rohleder, M., Pfaff, L., Kowarschik, M., Birkhold, A., Maier, A., 2023. Transient hemodynamics prediction using an efficient octree-based deep learning model, in: Frangi, A., de Bruijne, M., Wassermann, D., Navab, N. (Eds.), *Information Processing in Medical Imaging, Springer Nature Switzerland, Cham*. pp. 183–194.
- Morales Perez, X., Mill, J., Juhl, K.A., Acebes, C., Iriart, X., Legghe, B., Cochet, H., De Backer, O., Paulsen, R.R., Camara, O., 2021. Deep learning framework for real-time estimation of in-silico thrombotic risk indices in the left atrial appendage. *Frontiers in Physiology* 12.
- Nannini, G., Saitta, S., Mariani, L., Maragna, R., Baggiano, A., Mushtaq, S., Pontone, G., Redaelli, A., 2024. An automated and time-efficient framework for simulation of coronary blood flow under steady and pulsatile conditions. *Computer Methods and Programs in Biomedicine* 257, 108415.
- Park, J., Florence, P., Straub, J., Newcombe, R., Lovegrove, S., 2019. Deepsdf: Learning continuous signed distance functions for shape representation, in: *2019 IEEE/CVF Conference on Computer Vision and Pattern Recognition (CVPR)*, IEEE Computer Society, Los Alamitos, CA, USA. pp. 165–174.
- Paszke, A., Gross, S., Massa, F., Lerer, A., Bradbury, J., Chanan, G., Killeen, T., Lin, Z., Gimelshein, N., Antiga, L., Desmaison, A., Köpf, A., Yang, E., DeVito, Z., Raison, M., Tejani, A., Chilamkurthy, S., Steiner, B., Fang, L., Bai, J., Chintala, S., 2019. PyTorch: an imperative style,

- high-performance deep learning library, in: Proceedings of the 33rd International Conference on Neural Information Processing Systems, Curran Associates Inc., Red Hook, NY, USA. p. 0–12.
- Pegolotti, L., Pfaller, M.R., Rubio, N.L., Ding, K., Brugarolas Brufau, R., Darve, E., Marsden, A.L., 2024. Learning reduced-order models for cardiovascular simulations with graph neural networks. *Computers in Biology and Medicine* 168, 107676.
- Pontone, G., Moharem-Elgamal, S., Maurovich-Horvat, P., Gaemperli, O., Pugliese, F., Westwood, M., Stefanidis, A., Fox, K.F., Popescu, B.A., 2017. Training in cardiac computed tomography: EACVI certification process. *European Heart Journal - Cardiovascular Imaging* 19, 123–126.
- Qi, C.R., Yi, L., Su, H., Guibas, L.J., 2017. PointNet++: Deep hierarchical feature learning on point sets in a metric space, in: Guyon, I., von Luxburg, U., Bengio, S., Wallach, H.M., Fergus, R., Vishwanathan, S.V.N., Garnett, R. (Eds.), *Advances in Neural Information Processing Systems 30: Annual Conference on Neural Information Processing Systems 2017, December 4-9, 2017, Long Beach, CA, USA*, pp. 5099–5108.
- Rabe, M.N., Staats, C., 2021. Self-attention does not need $O(n^2)$ memory, in: n/a, pp. 1–8.
- Raissi, M., Perdikaris, P., Karniadakis, G., 2019. Physics-informed neural networks: A deep learning framework for solving forward and inverse problems involving nonlinear partial differential equations. *Journal of Computational Physics* 378, 686–707.
- Raissi, M., Yazdani, A., Karniadakis, G.E., 2020. Hidden fluid mechanics: Learning velocity and pressure fields from flow visualizations. *Science* 367, 1026–1030.
- Rygiel, P., Pluszka, P., Ziundefinedba, M., Konopczyński, T., 2023. Centerlinepointnet++: A new point cloud based architecture for coronary artery pressure drop and vfr estimation, in: *Medical Image Computing and Computer Assisted Intervention – MICCAI 2023: 26th International Conference, Vancouver, BC, Canada, October 8–12, 2023, Proceedings, Part VII*, Springer-Verlag, Berlin, Heidelberg. p. 781–790.
- Suk, J., Alblas, D., Hutten, B.A., Wiegman, A., Brune, C., van Ooij, P., Wolterink, J.M., 2024a. Physics-informed graph neural networks for flow field estimation in carotid arteries, in: n/a, pp. 1–10.
- Suk, J., Brune, C., Wolterink, J.M., 2023. Se(3) symmetry lets graph neural networks learn arterial velocity estimation from small datasets, in: Bernard, O., Clarysse, P., Duchateau, N., Ohayon, J., Viallon, M. (Eds.), *Functional Imaging and Modeling of the Heart*, Springer Nature Switzerland, Cham. pp. 445–454.
- Suk, J., de Haan, P., Lippe, P., Brune, C., Wolterink, J.M., 2024b. Mesh neural networks for se(3)-equivariant hemodynamics estimation on the artery wall. *Computers in Biology and Medicine* 173, 108328.
- Suk, J., Haan, P.D., Imre, B., Wolterink, J.M., 2024c. Geometric algebra transformers for large 3d meshes via cross-attention, in: *ICML 2024 Workshop on Geometry-grounded Representation Learning and Generative Modeling*, pp. 0–6.
- Suk, J., Imre, B., Wolterink, J.M., 2024d. Lab-gatr: geometric algebra transformers for large biomedical surface and volume meshes. *ArXiv abs/2403.07536*.
- Updegrave, A., Wilson, N.M., Merkow, J., Lan, H., Marsden, A.L., Shadden, S.C., 2017. SimVascular: An Open Source Pipeline for Cardiovascular Simulation. *Annals of Biomedical Engineering* 19, 525–541.
- Valen-Sendstad, K., Bergersen, A., Shimogonya, Y., Goubergrits, L., Bruening, J., Pallares, J., Cito, S., Piskin, S., Pekkan, K., Geers, A., Larrabide, I., Rapaka, S., Mihalef, V., Fu, W., Qiao, A., Jain, K., Roller, S., Mardal, K.A., Kamakoti, R., Spirka, T., Ashton, N., Revell, A., Aristokleous, N., Houston, J., Tsuji, M., Ishida, F., Menon, P., Browne, L., Broderick, S., Shojima, M., Koizumi, S., Barbour, M., Aliseda, A., Morales, H., Lefevre, T., Hodis, S., Al-Smadi, Y., Tran, J., Marsden, A., Vaippummadhom, S., Einstein, G., Brown, A., Debus, K., Niizuma, K., Rashad, S., ichiro Sugiyama, S., Khan, M., Updegrave, A., Shadden, S., Cornelissen, B., Majoie, C., Berg, P., Saalfeld, S., Kono, K., Steinman, D., 2018. Real-world variability in the prediction of intracranial aneurysm wall shear stress: The 2015 international aneurysm cfd challenge. *Cardiovascular engineering and technology* 9, 544–564.
- Vaswani, A., Shazeer, N., Parmar, N., Uszkoreit, J., Jones, L., Gomez, A.N., Kaiser, L., Polosukhin, I., 2017. Attention is all you need, in: Guyon, I., von Luxburg, U., Bengio, S., Wallach, H.M., Fergus, R., Vishwanathan, S.V.N., Garnett, R. (Eds.), *Advances in Neural Information Processing Systems 30: Annual Conference on Neural Information Processing Systems 2017, December 4-9, 2017, Long Beach, CA, USA*, pp. 5998–6008.
- Wang, S., Wu, D., Li, G., Zhang, Z., Xiao, W., Li, R., Qiao, A., Jin, L., Liu, H., 2023. Deep learning-based hemodynamic prediction of carotid artery stenosis before and after surgical treatments. *Frontiers in Physiology* 13, 1094743.
- Wu, K., Wu, E., Theodorou, B., Liang, W., Mack, C., Glass, L., Sun, J., Zou, J., 2024. Characterizing the clinical adoption of medical AI devices through U.S. insurance claims. *NEJM AI* 1, AIoa2300030. [arXiv:https://ai.nejm.org/doi/pdf/10.1056/AIoa2300030](https://ai.nejm.org/doi/pdf/10.1056/AIoa2300030).
- Xie, Y., Takikawa, T., Saito, S., Litany, O., Yan, S., Khan, N., Tombari, F., Tompkin, J., Sitzmann, V., Sridhar, S., 2022. Neural fields in visual computing and beyond. *Computer Graphics Forum* 41, 641–676.
- Zhang, X., Mao, B., Che, Y., Kang, J., Luo, M., Qiao, A., Liu, Y., Anzai, H., Ohta, M., Guo, Y., Li, G., 2023. Physics-informed neural networks (pinns) for 4d hemodynamics prediction: An investigation of optimal framework based on vascular morphology. *Computers in Biology and Medicine* 164, 107287.
- Zingaro, A., Vergara, C., Dede, L., Regazzoni, F., Quarteroni, A., 2023. A comprehensive mathematical model for cardiac perfusion. *Scientific Reports* 13.